Science Advances
AAAS

advances.sciencemag.org/cgi/content/full/5/4/eaav4803/DC1

Supplementary Materials for

Synthetic and living micropropellers for convection-enhanced nanoparticle transport

S. Schuerle, A. P. Soleimany, T. Yeh, G. M. Anand, M. Häberli, H. E. Fleming, N. Mirkhani, F. Qiu, S. Hauert, X. Wang, B. J. Nelson, S. N. Bhatia*

*Corresponding author. Email: sbhatia@mit.edu

Published 26 April 2019, *Sci. Adv.* **5**, eaav4803 (2019)
DOI: 10.1126/sciadv.aav4803

The PDF file includes:

Other Supplementary Material for this manuscript includes the following:

(available at advances.sciencemag.org/cgi/content/full/5/4/eaav4803/DC1)

Movie S8 (.mov format). Tracking of swarms of NP transported by MTB induced fluid flow.
Movie S9 (.mov format). Fluorescent NP guided by fluid flow coupling to rotating swarms of bacteria.
Movie S10 (.mp4 format). Control of green fluorescently labeled MTB in microfluidic device.

Supplementary Text

Eulerian computational modeling

COMSOL Multiphysics was used as a finite element (FE) solver to analyze the fluid flow and particle distribution inside the microfluidic chips. The Fluid Flow interface was employed to solve the equations governing incompressible flow and the Transport of Diluted Species interface was used to solve the transport equation for the nanoparticles (NPs). The medium inside the channel was defined to be water ($\rho = 1000\,\frac{\mathrm{kg}}{\mathrm{m}^3}, \eta = 0.001\ \mathrm{Pa}\cdot\mathrm{s}$), whereas the collagen area was modeled as an arbitrary viscous fluid with a density of $\rho = 1400\,\frac{\mathrm{kg}}{\mathrm{m}^3}$ and dynamic viscosity of $\eta = 8\ \mathrm{Pa}\cdot\mathrm{s}$. The ABF, located in the middle of the channel with its axis parallel to the direction of flow, equidistant from the inlet and the outlet, was modeled as a rotating geometry with a rotational frequency ω of 10 Hz.

1.1. Boundary conditions

In order to numerically describe the flow field inside the chip, appropriate boundary conditions reflective of the experimental setup must be applied at each boundary. For fluid flow boundary conditions, a laminar velocity profile with an average velocity magnitude u of $25\,\frac{\mu\mathrm{m}}{\mathrm{s}}$ was assumed at the inlet, constant pressure was assumed at the channel outlet, and all walls were modeled as no-slip boundaries.

For boundary conditions applied to the transported species, a constant NP concentration of $1\,\frac{\mathrm{mol}}{\mathrm{m}^3}$ was set as the inflow condition, while a general outflow boundary condition was employed at the outlet, an assumption consistent with the expected dominance of convective transport for particles inside the channel. In addition to the no-slip boundary condition at the PDMS walls, a no-flux condition was also applied to the walls when solving the mass transport equation. The diffusion coefficient in collagen gels at the given concentration of 3% was taken from experimental data found in literature to be $D = 2.7 \times 10^{-13}\,\frac{\mathrm{m}^2}{\mathrm{s}}$ for particles with radius of r_p=100 nm (d_p=200 nm).[42]

1.2. Governing equations

Two distinct Reynolds numbers, i.e. rotational (Re_r) and translational (Re_t), can be defined in such cases where both a pipe flow and rotating machinery is present

$$Re_t = \frac{\rho u d_c}{\eta} \approx 1.5 \times 10^{-3}$$
$$Re_r = \frac{\rho \omega d_h^2}{\eta} \approx 6 \times 10^{-3}$$

where ρ is the density and η is the viscosity of water, d_c describes the channel hydraulic diameter, and d_h is the helix (ABF) diameter located inside the channel.

Since both $Re_t \ll 1$and $Re_r \ll 1$, fluid flow is in the Stokes regime, even in the vicinity of the ABF. The ratio between the rotational Reynolds number and the translational Reynolds number helps to explain the convection enhancement effect due to the ABF inside the chip. Another non-dimensional parameter that must be evaluated is the Stokes number St, which characterizes the extent to which particles follow streamlines describing flow. This tests the validity of using the mass transport equation for the NPs

$$St = \frac{\tau u}{d_c}$$

In which the relaxation time τ is calculated as follows

$$\tau = \frac{\rho d_p^2}{18\eta}$$

Therefore, in the given case, the Stokes number can be obtained by

$$St = \frac{\rho_p d_p^2 u}{18 \eta d_c} \approx 0.01$$

in which ρ_p and d_p are particles' density and diameter, respectively.

Considering the value of the Stokes number ($St \ll 1$), it can be asserted that particles generally follow the streamlines. Thus, solving the transport equation to calculate the distribution of NPs was considered to be an appropriate method to capture these characteristics. Note that density and viscosity values of the water are used again in the calculation.

The final non-dimensional parameter that provides insight into this problem is the Peclet number. This number shows the relative contribution of convective transport to diffusive transport. Again, two Peclet numbers can be defined in this case based on translational and rotational velocity magnitudes

$$Pe_t = \frac{Lu}{D} \approx 90$$
$$Pe_r = \frac{L \omega d_h}{D} \approx 2200$$

where L represents the characteristic length scale of the channel, which in this case is the channel's height.

The magnified convective transport is clearly seen by comparing the above values. It should be noted that the Peclet number is also significant in the context of the stability of the numerical scheme. It has been mathematically proven that numerical instabilities occur when the element Peclet number exceeds 1. Thus, the maximum allowable mesh size h_{max} is determined by taking the highest velocity magnitudes in the domain into account. Substituting the swirl velocity of the ABF, the highest velocity in this problem, into the Pe number definition, one can obtain

$$Pe = \frac{h_{max} \cdot \omega d_h}{D} = 1 \rightarrow h_{max} = \frac{D}{\omega d_h} \approx 30 \text{ nm}$$

Fulfilling this condition in the meshing process leads to a substantial increase in the number of required computations and the runtime for the simulation. Therefore, stabilization methods have been used in combination with an adaptive mesh based on the approximate values of velocity magnitudes to numerically solve the mass transport equation with the FE solver.

Lagrangian computational modeling

The Particle Tracing interface of the COMSOL Multiphysics was used to model the particles' motion inside the channel under the influence of convective effects in a simplified 2D model, now considering momentum of the particles and the influence exerted by forces acting upon them such as drag and lift. The Basset–Boussinesq–Oseen equation (BBO equation) describes the motion of particles in the fluid flow. The diameter and density of the particles were set to 200 nm and 1060 $\frac{kg}{m^3}$, respectively. The same inlet velocity as the real 3D geometry was set as the boundary condition for the model. The small rectangle inside the channel acts as an artificial flow generator, which produces the same perpendicular velocity as the ABF, assuming the diameter and rotational frequency of the ABF in the real case.

Supplementary Figures

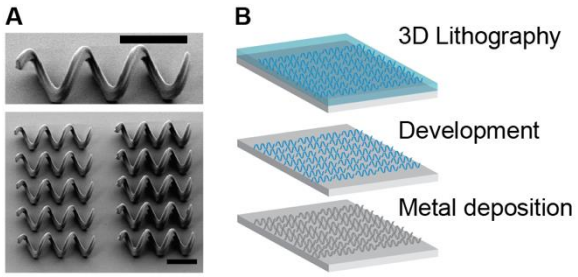

Fig. S1. ABF fabrication process. A Scanning electron micrographs of ABFs (scale bar = 15 µm).
B Schematic of fabrication process beginning with 3D lithography using the Nanoscribe® laser lithography system. Blue indicates the IP-L photoresist layer and dark blue represents the exposed areas that remain after the resist development process and washing. Finally, the structures are coated with a layer of titanium and nickel.

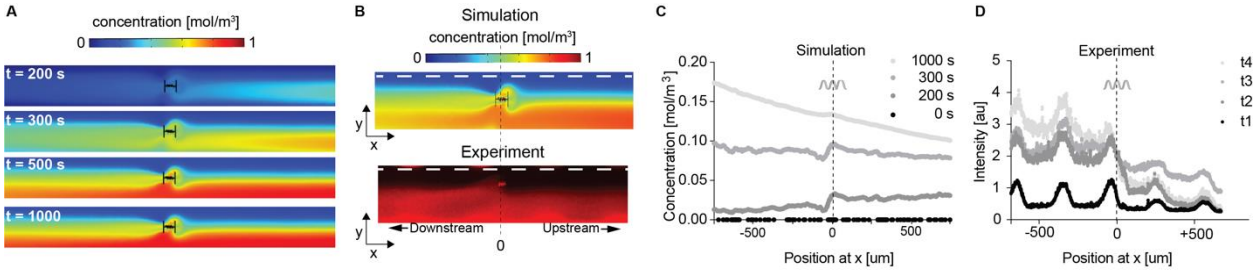

Fig. S2. Experimental results and simulations in 200-µm-wide channels. A Simulation of ABF in 2-fluid-flow channel. At t=0, the two fluids are injected into the channel, the progression of mixing by the ABF is illustrated by the snapshots at increasing time points towards steady state. **B**. Image of an ABF in 2-fluid-flow channel (bottom) and result of simulation (top) depicting the concentration distribution at steady state with the ABF in the center of the channel. The top fluid is water while the bottom fluid is a dense solution of red fluorescent labelled NP, simulated as molecular species with same diffusion coefficient. The concentration or fluorescence intensity, were measured either in silico or in vitro, respectfully, along the white dotted lines over time. **C** The concentration at this dotted line increases over time as shown in the simulation. The concentrated fluid from the bottom is moved up and mixed with the separated stream of water. **D** A similar profile was observed in experiments. The NP concentration is increasing over time (from t1=15s, t=25s, t3= 150s to t4=260s) as the ABF is transporting NPs from the lower fluid channel to the upper stream.

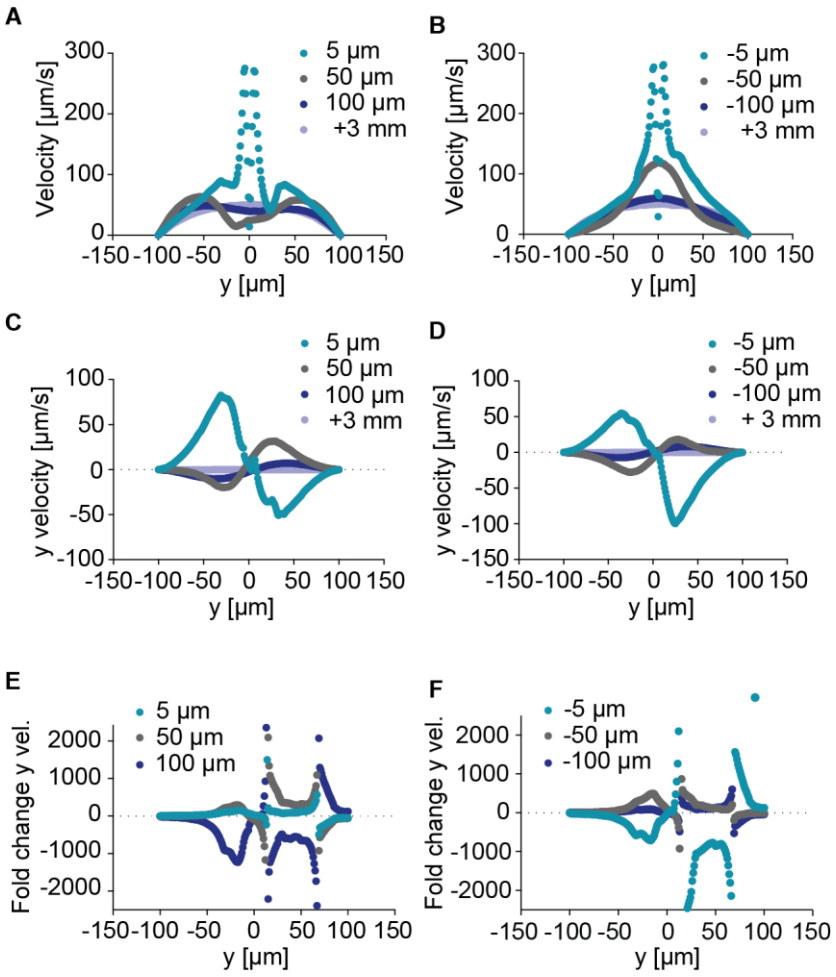

Fig. S3. ABF perturbs local fluid flow and increases total fluid velocity. A Velocity profile at distinct positions upstream of the ABF. For the control, at x= 3mm, an unperturbed laminar profile with peak velocity of 50 µm/s was simulated. At x = 100 and x = 50 µm upstream of the ABF, an increase of peak velocities is not only suggested, but the peak is also shifted closer toward the channel wall. **B** Velocity profile at distinct positions downstream of the ABF. A substantial increase in peak velocities is predicted. **C** Simulation results for effect on y velocity component $\mathbf{u}_y$ (orthogonal to and out of the channel) upstream of the ABF at x=5, x=50, and x=100 µm compared to the y velocity at x=3 mm upstream (internal control). In the vicinity of the ABF, a push directed outside of the channel, orthogonal to the flow direction, was observed. **D** Measurement of y velocity profile downstream of the ABF at x=-5, x=-50, and x=-100 µm). **E**, **F** Effect on Péclet number. Higher observed velocities result in higher ratios of convective to diffusive transport, formalized by an overall increase of the Péclet number. Regarding only the y velocity component of that ratio, an increase of over 2000-fold was measured in the vicinity of the ABF, both upstream (E) and downstream (F).

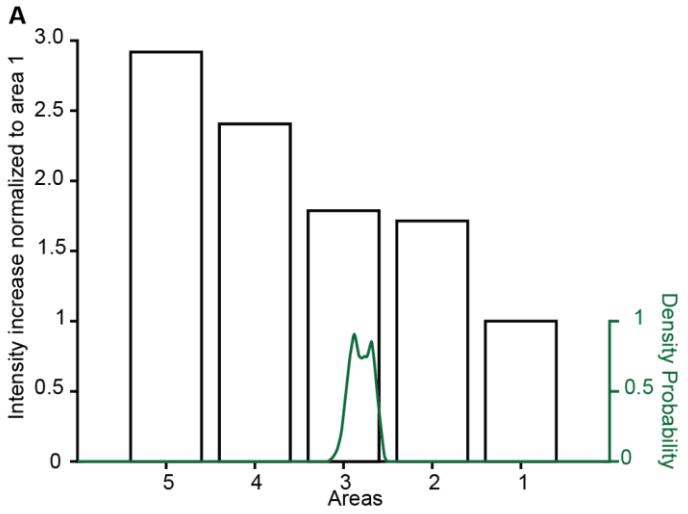

Fig. S4. Effect of ABF and position control. A typical distribution of intensity change over time (normalized to area 1) is shown. The areas 2-5 show increased NP accumulation over time compared to area 1. The probability density for the position of the ABF over the course of the experiment is depicted in green, showing its narrow position control around the center outlet area 3.

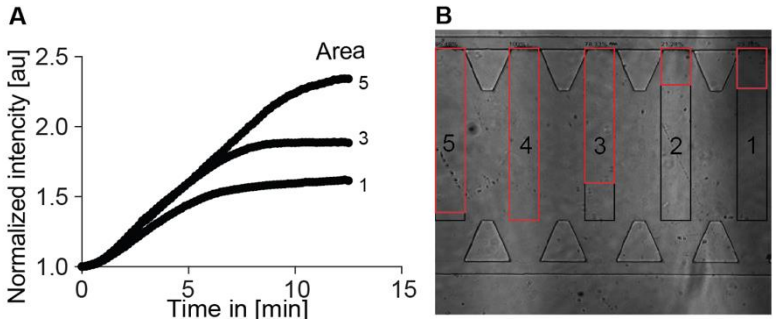

Fig. S5. Intensity increase over time. A Results of an experiment comparing the increase of fluorescence intensity over time for the outlet area at the ABF (3) and downstream (5) compared to area 1, which serves as an internal baseline. **B** Bright field image of ABF during the experiment in 50µm wide channel. Red overlays show the relative intensity increase (here with respect to the maximum = outlet 4) recorded in the outlined region of interest.

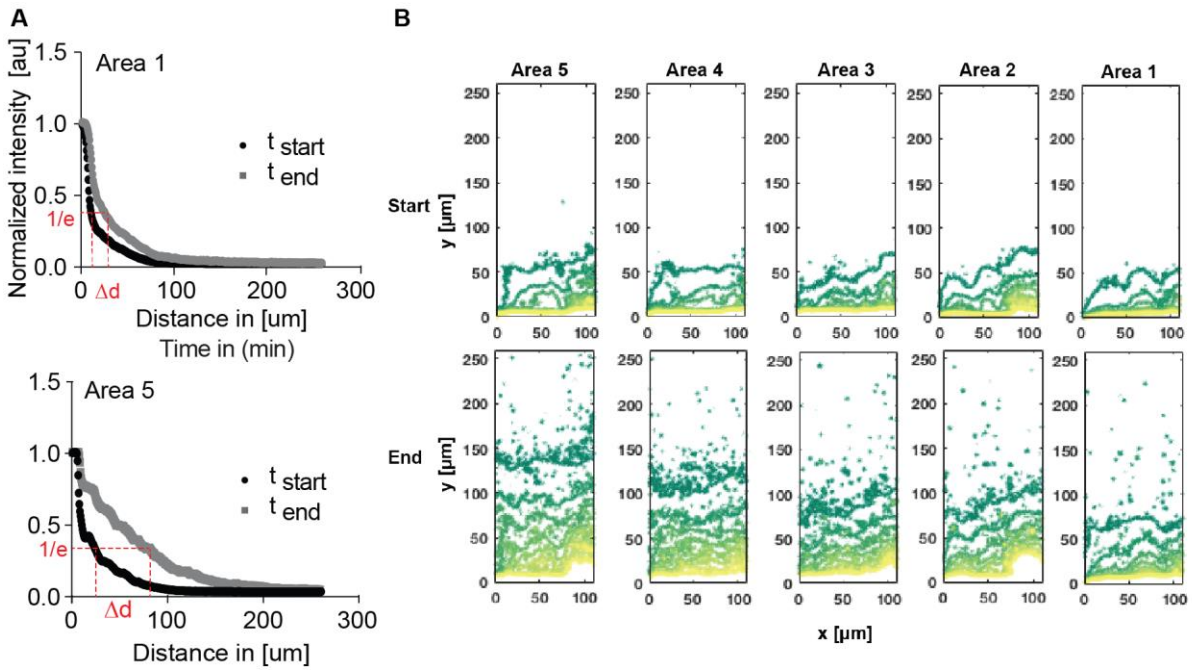

Fig. S6. Plots of NP penetration depth increase over time influenced by ABF. A The fluoresence intensity over the distance away from the channel wall was measured at the beginning and end of an experiment. The overall increase in penetration depth ***Δ***d was then quantified by measuring the distance at which fluorescence intensity fell to 1/e of its maximum value at the channel wall. As shown in detail in individual graphs for outlet Area 1 (top) and Area 5 (bottom), only a slight increase is seen in the Area 1 compared to the increase in Area 5 that was influenced by the ABF. **B** The top row shows NP distribution as intensity distribution in the respective collagen outlet areas 1-5 (yellow=high intensity, green = low intensity) at the beginning of the experiment. The bottom row shows the respective areas after the actuation experiment and higher intensity levels deeper along y into the collagen area are measured.

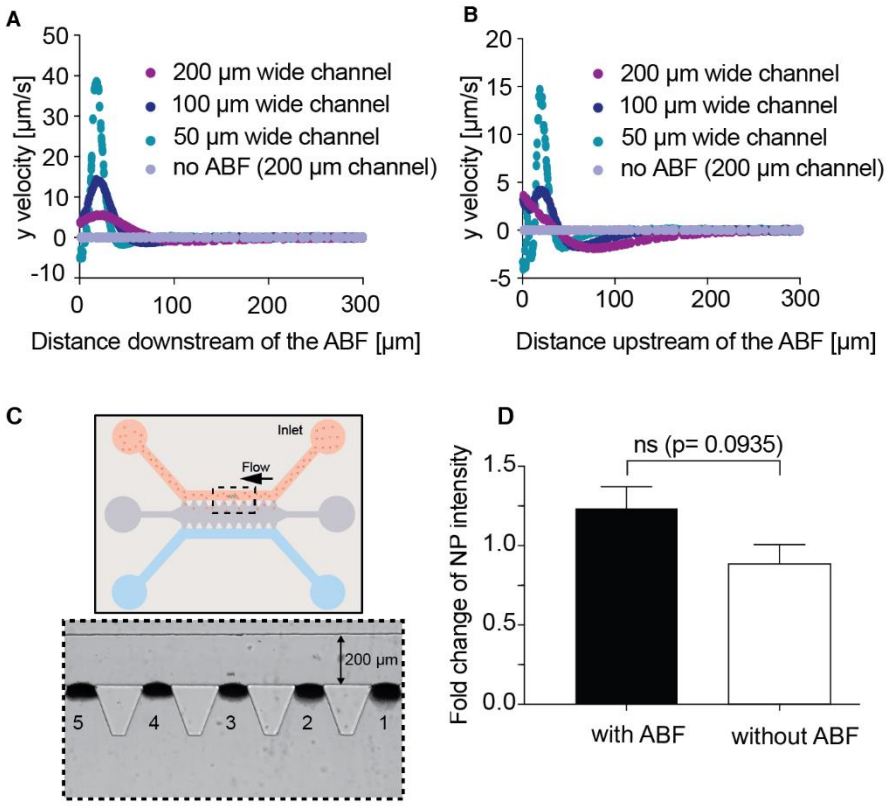

Fig. S7. Effect of channel diameter. The graphs show the effect of channel diameter on fluid flow velocities perpendicular to the incoming flow up downstream (**A**) and upstream of the ABF (**B**). **C**, **D** Experimental results in 200 µm channels under 1-fluid flow. A schematic of the device is depicted in C and the fold change of NP intensity in outlet areas 2-5 over 1 for devices with and without and ABF is plotted in D showing that the effect is weak in larger channels (n=5).

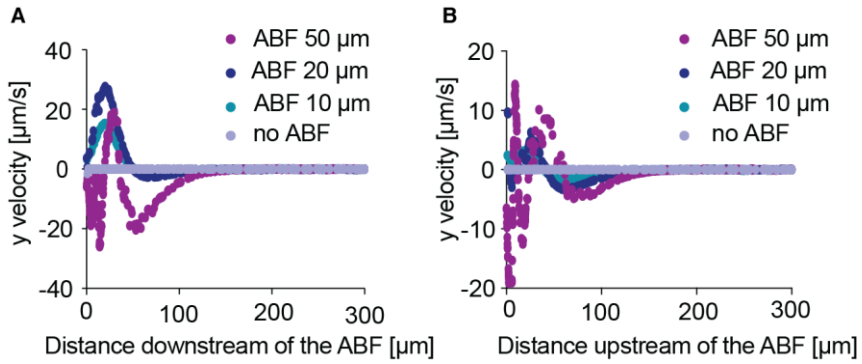

Fig. S8. Effect of ABF diameter. These results are derived from simulations in a 200 µm wide channel where we investigated the effect of the ABF diameter on distortion of the fluid flow. The graphs show the effect of the diameter of the ABF on fluid flow velocities perpendicular to the incoming flow (y velocity component) up (**A**) downstream and (**B**) upstream of the ABF. The fluid flow is more increased for larger ABFs and the effect measurable at larger distance s away from the ABF. Overall, the magnitude of flow distortion is much smaller than compared to a channel of 50 µm in diameter (see fig. S9).

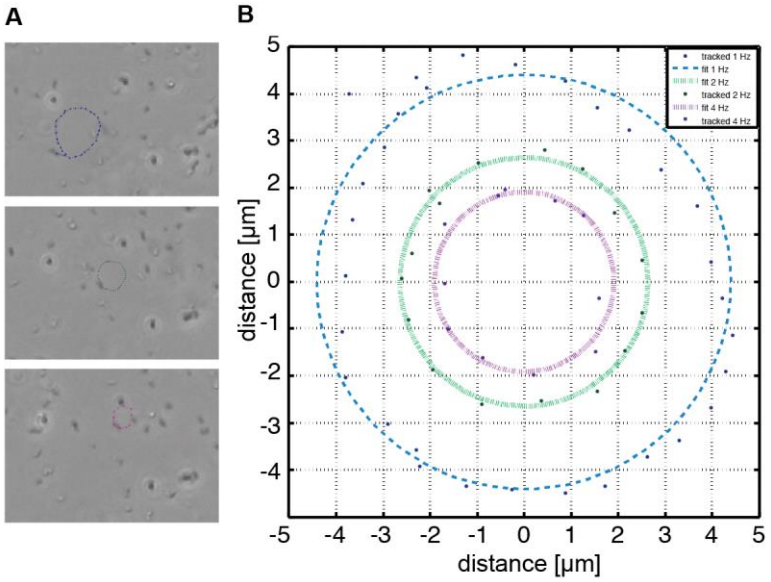

Fig. S9. Control of motile MTB with rotational fields in plane. A Tracked trajectories of MTB under fields with increasing rotational frequency (top to down). **B** Tracked positions and fitted circular trajectories for the different rotational velocities.

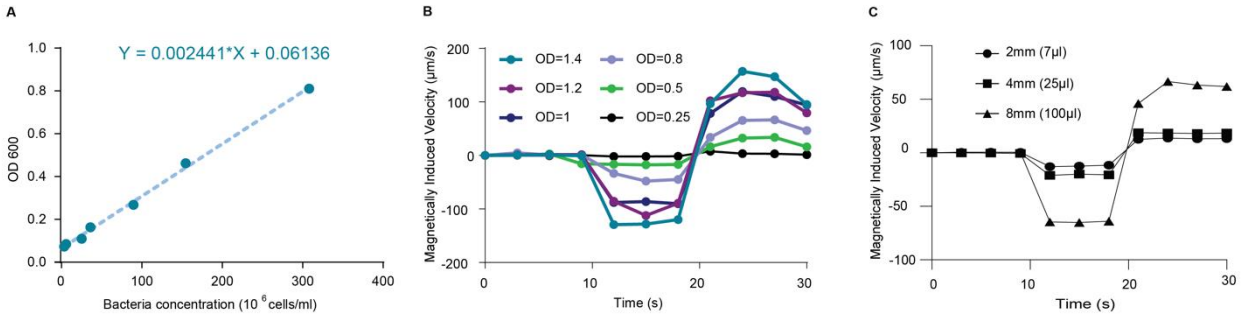

Fig. S10. Density effect. Measurement of translational velocities in samples with decreasing optical density and thus bacterial concentration. (**A**) Graph displaying the linear relationship between absorbance measurements at 600 nm wavelength (OD600) and concentration of bacteria. OD600 measurements were taken prior to all experiments to determine the concentration bacteria used. (**B**) Experimental results of translational fluid velocity at different densities of bacteria, under the same rotational magnetic field input. (**C**) Experimental results for translational fluid velocity in different sized cylindrical compartments of 2mm, 4mm, and 8mm diameter (i.e. under different spatially constrained conditions). While the translational velocity is higher in larger spaces (8mm in diameter), an observable transitional velocity is maintained also in the compartments of smaller size.

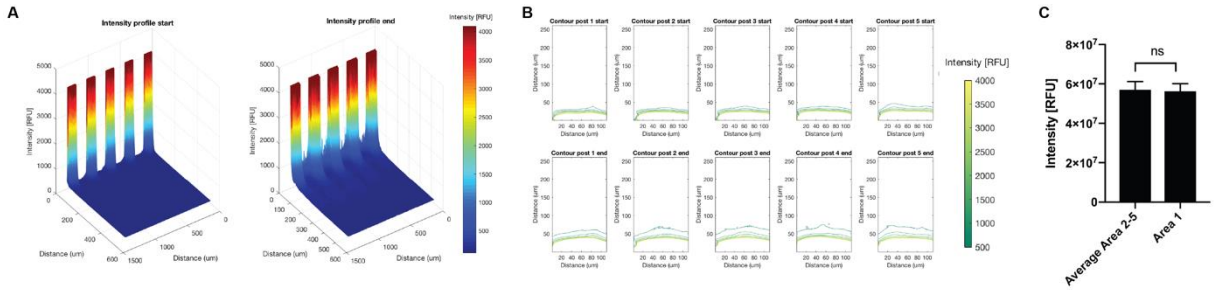

Fig. S11. MTB promotes homogenous transport enhancement. (**A**) Graph showing the homogenous intensity increase measured across one larger region of interest covering 5 outlet areas at start and end of a MTB experiment. (**B**) Graphs showing the homogenous intensity increase in the respective five outlet areas, as analyzed for experiments with ABF (**C**) As expected, due to the homogenous distribution of MTB along the channel, no significant difference in the mean intensity of Areas 2-5 compared to Area 1 for MTB experiment was found. Consequently, instead of analyzing against Area 1 as an internal control, transport experiments were analyzed by summing the intensity changes over all five areas and comparing experiments where a rotating magnetic field was applied (+RMF) with control experiments where no magnetic was applied (-RMF).

Supplementary Movies

Movie S1. Swimming of ABF through dense NP solution along S shape.

Movie S2. Swimming of ABF in two-fluid flow device.

Movie S3. Zoom of ABF swimming in two-fluid flow device.

Movie S4. ABF in one-fluid flow device.

Movie S5. Control of a single, motile MTB under static magnetic fields.

Movie S6. Control of swarm MTB under RMFs in-plane and out-of-plane.

Movie S7. Control of swarm MTB (red) mixed with nonmagnetic *Escherichia coli* (green) under RMFs.

Movie S8. Tracking of swarms of NP transported by MTB induced fluid flow.

Movie S9. Fluorescent NP guided by fluid flow coupling to rotating swarms of bacteria.

Movie S10. Control of green fluorescently labeled MTB in microfluidic device.